Optical Materials 95 (2019) 109237

Contents lists available at ScienceDirect

Optical Materials

journal homepage: www.elsevier.com/locate/optmat

NUV light-induced visible green emissions of Erbium-doped hierarchical $Bi_2Zr_2O_7$ structures

A.S. Rajashekharaiah[a,b], G.P. Darshan[c], R.B. Basavaraj[a], Yashwanth V. Naik[a], D. Kavyashree[d], S.C. Sharma[e,1], H. Nagabhushana[a,*]

[a] Prof. C.N.R. Rao Centre for Advanced Materials, Tumkur University, Tumkur 572 103, India
[b] Department of Physics, Govt. First Grade College, Tiptur, Tumkur 572 201, India
[c] Department of Physics, Acharya Institute of Graduate Studies, Bangalore 560 107, India
[d] Department of Physics, Acharya Institute of Technology, Bangalore 560 107, India
[e] National Assessment and Accreditation Council, Jain University, Bengaluru, India

ARTICLE INFO

Keywords:
Nanophosphor
Photoluminescence
Photometric properties
Dosimetry
Optical thermometry

ABSTRACT

We reported a facile strategy to synthesis of Er^{3+} doped $Bi_2Zr_2O_7$ nanophosphors via hydrothermal route using *Aloe Vera* gel as a bio - surfactant. The photoluminescence spectra exhibit intense peaks centered at ~524, 547 and 660 nm, which were attributed to $^2H_{11/2} \rightarrow {}^4I_{15/2}$, $^4S_{3/2} \rightarrow {}^4I_{15/2}$ and $^4F_{9/2} \rightarrow {}^4I_{15/2}$ transitions of Er^{3+} ions, respectively. The highest photoluminescence intensity was achieved in 5 mol % of Er^{3+} ions. The electric dipole-quadrupole (d-q) interaction was responsible for the concentration quenching. The fluorescence intensity ratio technique was utilized for optical thermometric properties of the nanophosphors in the temperature range of 303–463 K. At lower temperature (282 K) the relative sensor sensitivity of the optimized nanophosphor was found to be ~0.0621 K^{-1}. Thermoluminescence glow curves of 5 mol % Er^{3+} ions doped nanophosphor irradiated with γ-rays showed two peaks at ~120 and 203 °C. A thermoluminescence glow peak at ~120 °C showed good linearity with dose, simple glow curve structure, minimal fading and good reproducibility. The above results clearly showed that the optimized nanophosphor is quite useful in WLED's, TL dosimetry and optical thermometry applications.

1. Introduction

In recent years, nanomaterials (NMs) create numerous interest for the research community due to its widespread applications in many fields, namely medicine, energy, electronics, biotechnology, etc. [1–3]. Till now, various chemical and physical routes were followed for the synthesis of nanomaterials. For these routes, it requires sophisticated equipments, high temperature and vacuum environment. The most of the available chemical synthesis routes suffer elevated biological risks owing to use of toxic chemical reagents [4,5]. Therefore, preparation of NMs by utilizing various biogenic sources, namely plants, algae and microorganisms creates a new avenue in the current materials research [6]. Among, the phytosynthesis routes, the plant based extracts (root, leaf, stem etc.) exhibit numerous advantages such as eco-friendly, cost effective and bulk preparation [7,8]. From the literature, many plant extracts were used to synthesis nanomaterials. Among, the plant, Aloe *Vera* (*A.V.*) belongs to the *Liliaceae* family, which comprises major potential constituents, namely vitamins (including B1, B2, B3, B6, B12), minerals (such as calcium, magnesium, phosphorus, potassium, manganese, chromium, sodium, copper, zinc, iron and nitrogen), salicylic acids, enzymes, polysaccharides, sugars, amino acids, flavones, alkaloids, etc. [9]. Further, it has highly useful in medical applications, such as antifungal, anticancer activity, wound healing, hypoglycemic, etc. [10]. The use of *A.V.* extract as a bio-surfactant which benefit for the synthesis of various hierarchical structures which in turn enhance the luminescence properties as compared to conventional synthesis routes [11].

Nowadays, various inorganic metal oxides have created much attention owing to their excellent chemical and physical properties in widespread fields, namely anti-oxidant, solid state lighting, sensors, anticancer activity, and cell imaging [12–15]. Among, zirconates having the general formula $A_2Zr_2O_7$ creates much interest for scientific community due to its potential applications in various fields, namely photoelectrochemical catalyst, nuclear material, magneto

* Corresponding author.
E-mail address: bhushanvlc@gmail.com (H. Nagabhushana).
[1] Director, National Assessment and Accreditation Council, Bangalore, 560 072, India [work carried out as Honorary Professor, Jain University, Bengaluru, India].

https://doi.org/10.1016/j.optmat.2019.109237
Received 18 March 2019; Received in revised form 27 June 2019; Accepted 4 July 2019

Table 1
List of different synthesis routes employed for the preparation of $Bi_2Zr_2O_7$ material by various workers.

SI. No	Sample	Synthesis route	Reference
1	$Bi_2Zr_2O_7$	Co-precipitation	Yijia Luo et al. [17]
2	$Bi_2Zr_2O_7$	Co-precipitation	Yijia Luo et al. [18]
3	$Bi_2Zr_2O_7$	Soft-template sol-gel	Xiaowei Liu et al. [19]
4	Ag/AgI modified $Bi_2Zr_2O_7$	Precipitation & photo-reduction process	Tingting He et al. [20]
5	Ag/Agcl/$Bi_2Zr_2O_7$	Precipitation & photo-reduction process	Tingting He [21]
6	$Bi_2Zr_2O_7$	Sedimentation –calcination method	Deyong Wu et al. [22]
7	$Bi_2Zr_2O_7$	Solution combustion	Vaishali M. Sharma et al. [23]

hydrodynamic power generation, etc. Normally, $A_2Zr_2O_7$ exhibit two isometric structures at ambient conditions based on an ionic radius ratio of $r(A^{3+})/r(Zr^{4+})$. Among, the pyrochlore structure with the Fd-3m space group was highly stable with the radius ratio in the range of $1.46 \leq r(A^{3+})/r(Zr^{4+}) \geq 1.78$. In typical pyrochlore structure, A and Zr cations are eight-coordinated and six-coordinated occupying with 16d and 16c sites, respectively, and the O has two crystallographically distinct oxygen sites (48f, 8b). However, the defect fluorite structure with Fm-3m space group display radius ratio greater than 1.46. The defect fluorite structural system has disordered cations and anions reside in 4a and 8c positions respectively, in which one eighth of the anion sites vacant as compared with the ideal fluorite structure (AX_2). The transition of phases from pyrochlore structure to the defect fluorite structure is an order-disorder transition, which involves the disordering of the anions among the 48f, 8b sites and the vacant 8a site, as well as the disordering of the cations at 16c and 16d sites [16]. Table 1 shows the synthesis of $Bi_2Zr_2O_7$ by various workers in different routes [17–23].

In the present work, novel $Bi_2Zr_2O_7$:Er^{3+} (1–11 mol %) nanophosphors (NPs) were synthesized by hydrothermal route using *A.V.* gel as a bio-surfactant. The morphological analysis was studied with respect to various hydrothermal conditions. The luminescence studies of the prepared samples were systematically studied and analyzed for its suitability in WLED's, radiation dosimetry and optical thermometry applications.

2. Experimental

2.1. Synthesis

The precursors used in the study are Zirconyl chloride octahydrate [$ZrOCl_2{\cdot}8H_2O$; 98%, Sigma Aldrich], Bismuth (III) nitrate pentahydrate [$Bi(NO_3)_3.5H_2O$; 98%, Sigma Aldrich], Erbium (III) nitrate pentahydrate [$Er(NO_3)_3.5H_2O$; 99.9%, Sigma Aldrich], Nitric acid [HNO_3; 70%, Sigma Aldrich] and *A.V.* gel used as a bio-surfactant. The *A.V.* gel was extracted as per literature reported elsewhere [24]. The proper stoichiometric amount of Zirconyl chloride, Bismuth (III) nitrate and Erbium (III) nitrate were well in deionised water using a magnetic stirrer. The pH of the resulting solution was adjusted to 2, 5, 7 and 9 with the addition of concentrated HNO_3 in a dropwise at the rate of 2 ml/min. Subsequently, different concentrations (5, 10, 15, 20, 25, 30 and 35 ml) of the *A.V.* gel extract were homogeneously dissolved in 200 ml Millipore water and added slowly to the resultant mixture. The final solution was transferred to Teflon lined hydrothermal bomb (180 ml capacity). The hydrothermal bomb was placed in a hot air oven maintained at a temperature (180 °C) for 12 h. The resultant product was carefully collected and washed several times using acetone and deionized water. Finally, the obtained product was dried at 80 °C for 20 h and used for further studies. Further, the experiment was repeated by varying different concentrations of Er^{3+} (1–11 mol %), temperature (120, 140, 160, 180, 200 °C) and reaction time (12, 24, 36, 48, 60 and 72 h). For all the above experimental conditions, the optimized *A.V.* gel concentration (35 ml) was maintained. The schematic representation for the preparation of $Bi_2Zr_2O_7$:Er^{3+} (1–11 mol %) NPs was shown in Fig. 1.

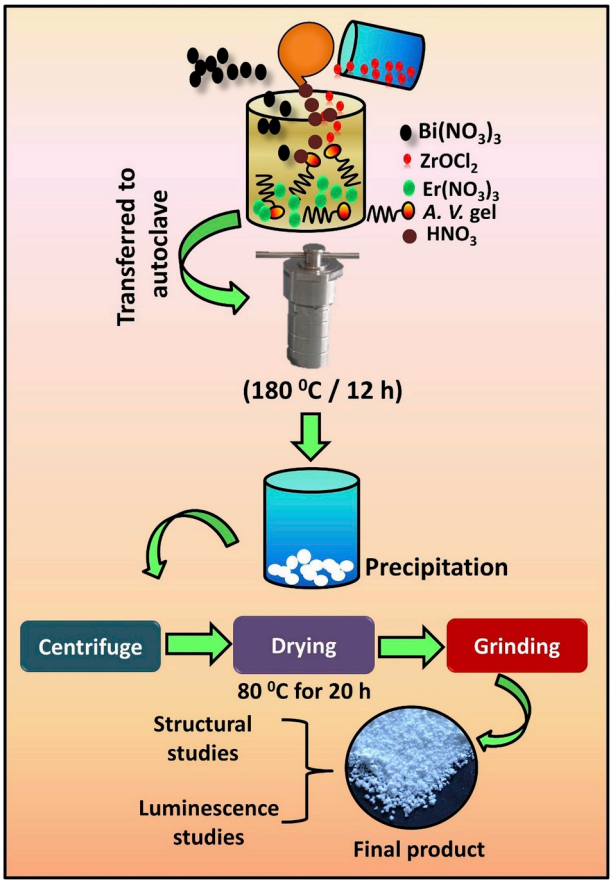

Fig. 1. Scheamtic illustration for hydrothermal syntehsis of $Bi_2Zr_2O_7$:Er^{3+} (1–11 mol %) NPs.

2.2. Characterization

The powder X-ray diffraction (PXRD) studies of the prepared NPs were examined in a Powder X-ray diffractometer (Shimadzu-7000). The morphology of the sample was studied by utilizing a scanning electron microscope (HITACHI-3000) and transmission electron microscope (JEOL). Diffuse reflectance (DR) spectral studies was performed by using the Lambda 35, UV/Vis spectrophotometer (PerkinElmer). Photoluminescence (PL) studies of the prepared NPs were examined using Horiba made spectrofluorimeter. Life time decay measurements were recorded with pulsed 355 nm laser (Nd^{3+}: YAG) radiation as an excitation source. Thermoluminescence (TL) studies were performed by irradiating the samples with ^{60}Co γ-rays in the dose range 1–6 kGy. The TL studies were examined using indigenous Nucleonix TL (Model 1009I) reader.

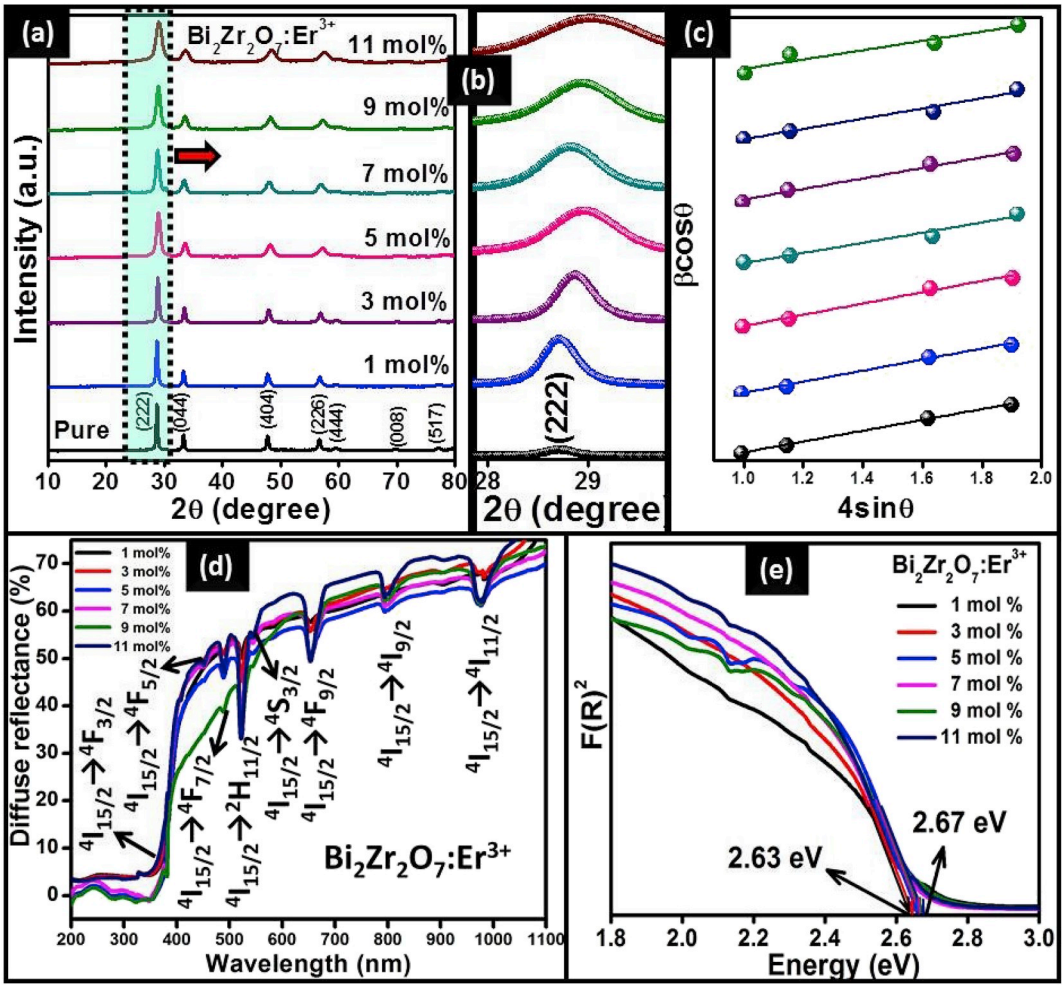

Fig. 2. (a) PXRD patterns, (b) magnified view of peak (222), (c) W–H plots, (d) DR spectra and (e) energy band gap plots of $Bi_2Zr_2O_7:Er^{3+}$ (1–11 mol %) NPs.

Table 2
Estimated crystallite size, strain and energy gap (E_g) values of $Bi_2Zr_2O_7:Er^{3+}$ (1–11 mol %) NPs.

Er^{3+} conc. (mol %)	Crystallite size (nm)		Strain (x 10^{-4})	E_g value (eV)
	[Scherrer's approach]	[W–H approach]		
1	21	24	1.4	2.63
3	20	23	1.7	2.64
5	18	21	1.8	2.65
7	19	20	1.4	2.65
9	16	17	1.9	2.66
11	15	16	1.8	2.67

3. Results and discussion

Fig. 2 (a) depicts the PXRD profiles of $Bi_2Zr_2O_7:Er^{3+}$ (1–11 mol %) NPs. The obtained PXRD peaks corresponds to the (222), (044), (404), (226), (444), (008) and (517) planes, which were in good agreement with the reported literature [22,23]. Absence of peak at ~15° showed the defect-fluorite structure of the prepared samples with $Fm\bar{3}m$-225 space group. No impurity peaks were noticed, indicating that dopant Er^{3+} ions were successfully incorporated into host $Bi_2Zr_2O_7$ site. A small shift in the diffraction (222) plane towards the larger angle side with increase of Er^{3+} ion concentration was noticed (Fig. 2 (b)), which due to ionic radii mismatch. The acceptable percentage difference (D_r) between the ionic radii of Bi^{3+} (1.17 Å) and dopant Er^{3+} (1.004 Å) ions was estimated using the relation described elsewhere [25]. The calculated D_r value was found to be ~14.18% (< 30 %), which indicate that Er^{3+} ions successfully substituted into the Bi ions site. The average crystallite size (D) of the prepared NPs was calculated by using both Scherrer's and Williamson-Hall (W–H) method using following relations [26];

$$D = \frac{0.9\lambda}{\beta \cos\theta} \quad (1)$$

$$\beta = \frac{K\lambda}{D \cos\theta} + 4\varepsilon \tan\theta \quad (2)$$

where, λ; wavelength of X-rays used, θ; Bragg's angle, β; full-width at half maximum and ε; lattice strain. The W–H plots of $Bi_2Zr_2O_7:Er^{3+}$ (1–11 mol %) NPs was shown in Fig. 2 (c). The estimated crystallite size (D) of the prepared NPs was listed in Table 2. As evident from the table, the estimated crystallite size decreases with increase of Er^{3+} concentration. In addition, the crystallite size assessed from W– H plots were found to be to somewhat higher than the values estimated using Scherrer's formula. Such variation in the crystallite size was due to the fact that the component of strain was assumed to be zero in the Scherrer's formula.

Fig. 2 (d) depicts the DR spectra of $Bi_2Zr_2O_7:Er^{3+}$ (1–11 mol %) NPs recorded in the range of 200–1100 nm. The spectra exhibit several absorption peaks at ~442 ($^4I_{15/2} \rightarrow {}^4F_{3/2}$), 451 ($^4I_{15/2} \rightarrow {}^4F_{5/2}$), 488 ($^4I_{15/2} \rightarrow {}^4F_{7/2}$), 521 ($^4I_{15/2} \rightarrow {}^2H_{11/2}$), 543 ($^4I_{15/2} \rightarrow {}^4S_{3/2}$), 660 ($^4I_{15/2} \rightarrow {}^4F_{9/2}$), 797 ($^4I_{15/2} \rightarrow {}^4I_{9/2}$) and 977 ($^4I_{15/2} \rightarrow {}^4I_{11/2}$) [27]. The Kubelka–Munk theory was utilized to estimate the energy band gaps (E_g)

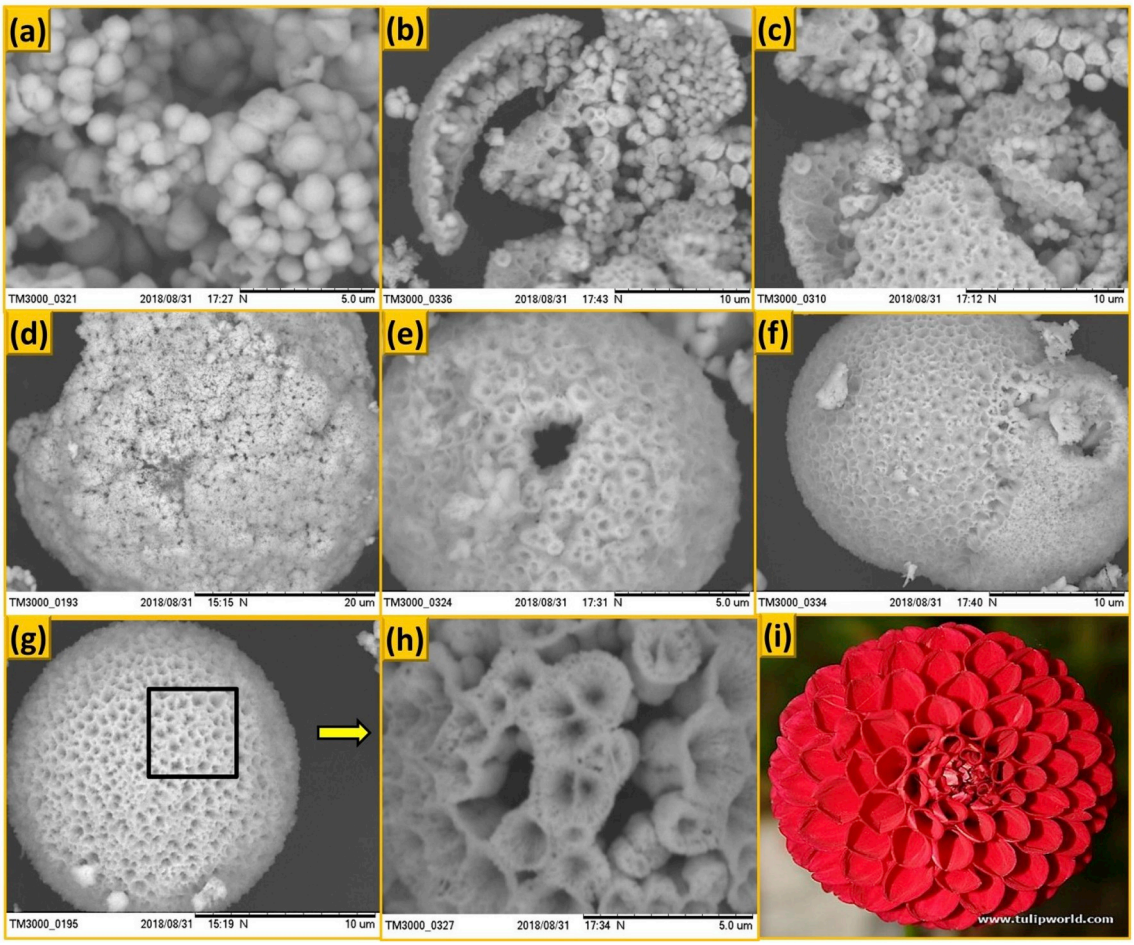

Fig. 3. SEM micrographs of $Bi_2Zr_2O_7:Er^{3+}$ (5 mol %) NPs prepared with different *A.V.* gel concentrations, (a) 5 ml, (b) 10 ml, (c) 15 ml, (d) 20 ml, (e) 25 ml, (f) 30 ml, (g) 35 ml, (h) enlarged portion of Fig. 3 (g) and (i) natural marigold flower.

of the prepared NPs based on the relations described elsewhere [28]. The energy band gaps of $Bi_2Zr_2O_7:Er^{3+}$ (1–11 mol %) NPs was depicted in Fig. 2 (e). The E_g values were estimated and listed Table 2. It was evident from the table that, the E_g values increases with increase of Er^{3+} ion concentration, which may due to the several structural order and disorder with the diverse experimental conditions.

Fig. 3 Shows SEM images of $Bi_2Zr_2O_7:Dy^{3+}$ (5 mol %) NPs synthesized with various concentrations of *A.V.* gel. It was evident from the figure that, when *A.V.* gel concentration was ~5 ml, individual spherical shaped particles were noticed (Fig. 3 (a)). Further, when the *A.V.* gel concentration was increased to 10–20 ml, individual particles adjoining together to form hollow spherical hierarchical structures (Fig. 3(b and c & d)). However, the concentration of *A.V.* gel increased to 25–35 ml, individual building blocks assembled together to form 3D hierarchical hallow spherical structures (Fig. 3(e–g)). The enlarged portion of SEM image of hallow spherical structure (Fig. 3 (h)), evident that its entire surface enclosed with small micro-flowers which resembles a natural marigold flower (Fig. 3 (i)).

SEM micrographs of the prepared $Bi_2Zr_2O_7:Dy^{3+}$ (5 mol %) NPs prepared with various reaction temperatures and fixed *A.V.* gel concentration (35 ml) was depicted in Fig. 4. When the hydrothermal temperature was maintained at ~120 °C, hallow spherical shape structure with more uneven concavities were observed (Fig. 4 (a)). Further, the reaction temperature was prolonged to 140 °C, a spherical structure with small inclines were noticed (Fig. 4 (b)). When the reaction temperature was elevated to 160 and 180 °C, 3D hallow spherical structures with big inclines clearly observed (Fig. 4(c and d)). The same hierarchical 3D spherical structure was retained with small micro-flowers on the surface directed outwards was clearly noticed, when the reaction temperature raised to 200 °C (Fig. 4 (e)).

Effect of hydrothermal reaction time (12, 24, 36, 48, 60 and 72 h) on morphology of the prepared $Bi_2Zr_2O_7:Dy^{3+}$ (5 mol %) NPs by fixed *A.V.* gel concentration (35 ml) and temperature (200 °C) was studied (Fig. 5). When the reaction time duration was maintained to 12 h, large number of small spherical structures with various sizes were clearly observed (Fig. 5 (a)). Further, the reaction time duration was prolonged to 24 and 36 h, the individual spherical structures undergo growth to form self-assembled larger sized spherical structure was noticed (Fig. 5(b and c)) With the increase of reaction time to 48 h, the spherical structure undergo Ostwald ripening to form non-uniform hierarchical bud-like structure (Fig. 5 (d)). Further, increase of reaction time in 60 and 72 h, the uniform hierarchical bud-like structure were clearly noticed (Fig. 5(e and f).

In addition to the above parameters, pH was another vital parameter which influences the morphology of the samples. The effect pH (2, 5, 7 and 9) on the morphology prepared $Bi_2Zr_2O_7:Dy^{3+}$ (5 mol %) NPs synthesized with optimized hydrothermal parameters (Fig. 6). At the initial pH of 2, irregular shaped quasi growth spherical structure was noticed (Fig. 6 (a)). When the pH level was increased to 5, individual spherical structures were clearly observed (Fig. 6 (b)). The pH level was further increased to 7, a self-assembly of individual structures was noticed (Fig. 6 (c)). Individual spherical structures acts as a building blocks were assembled to form hallow 3D spherical hierarchical structure was noticed, when the pH was set to 9 (Fig. 6 (d)).

TEM, HRTEM and SAED patterns of $Bi_2Zr_2O_7:Er^{3+}$ (5 mol %) NPs prepared with fixed *A.V.* gel concentration (35 ml) and temperature

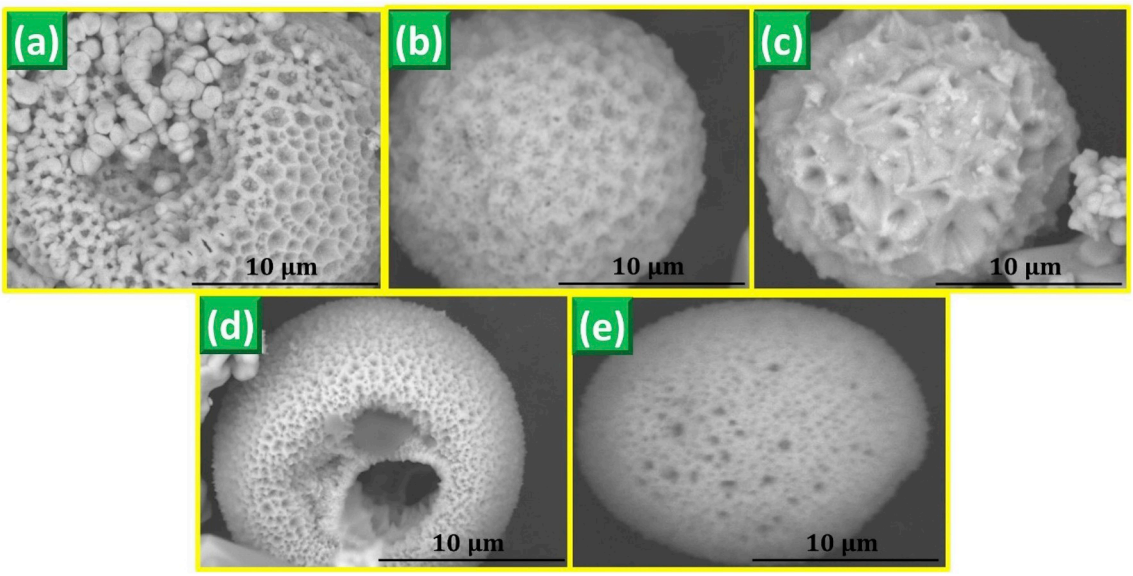

Fig. 4. SEM micrographs of $Bi_2Zr_2O_7:Er^{3+}$ (5 mol %) NPs synthesized with different reaction temperatures (120, 140, 160, 180 and 200 °C) and fixed *A.V.* gel concentration (35 ml).

(200 °C) was shown in Fig. 7. TEM images were clearly evidences spherical structure of the prepared NPs (Fig. 7(a and b)). The obtained results were in good agreement with corresponding SEM images. From HRTEM image, the interplanar spacing (d) was estimated and found to be ~0.29 and 0.31 nm for planes (222) and (044), respectively (Fig. 7 (c)). The diffraction rings with brighter spots in the SAED pattern confirmed the crystalline nature of the NPs (Fig. 7 (d)).

3.1. Photoluminescence studies

Fig. 8 (a) depicts the PL excitation spectrum of $Bi_2Zr_2O_7:Er^{3+}$ (5 mol %) NPs monitored at 547 nm emission wavelength. The spectrum exhibits intense peaks at ~364, 380, 405, 450 and 488 nm, which were attributed to $^4I_{15/2} \rightarrow {}^4G_{9/2}$, $^4I_{15/2} \rightarrow {}^4G_{11/2}$, $^4I_{15/2} \rightarrow {}^4H_{9/2}$, $^4I_{15/2} \rightarrow {}^4F_{5/2}$ and $^4I_{15/2} \rightarrow {}^4F_{7/2}$ transitions of Er^{3+} ions, respectively [29]. PL emission spectra of $Bi_2Zr_2O_7$: Er^{3+} (1–11 mol %) NPs excited at ~ 380 nm was shown in Fig. 8 (b). The spectra exhibit characteristic peaks at ~524, 547 and 660 nm, which were owing to $^2H_{11/2} \rightarrow {}^4I_{15/2}$, $^4S_{3/2} \rightarrow {}^4I_{15/2}$ and $^4F_{9/2} \rightarrow {}^4I_{15/2}$ transitions of Er^{3+} ions, respectively [30]. Variation of PL intensity with various concentrations of Er^{3+} ions was depicted in Fig. 8 (c). As can be seen from the figure that, the PL intensity gradually increases with increase of Er^{3+} concentration up to 5 mol % and later diminishes. This decrease in PL intensity was mainly due to well-known concentration quenching phenomena [31]. The concentration quenching was mainly caused by the non-radiative energy transfer among Er^{3+} ions, which normally arises as a result of an exchange interaction, radiation reabsorption, or a multipole–multipole interaction. Hence, critical distance (R_c) between the neighboring Er^{3+} ions were estimated in order to know the type of the interaction mechanism. According to Blasse's,

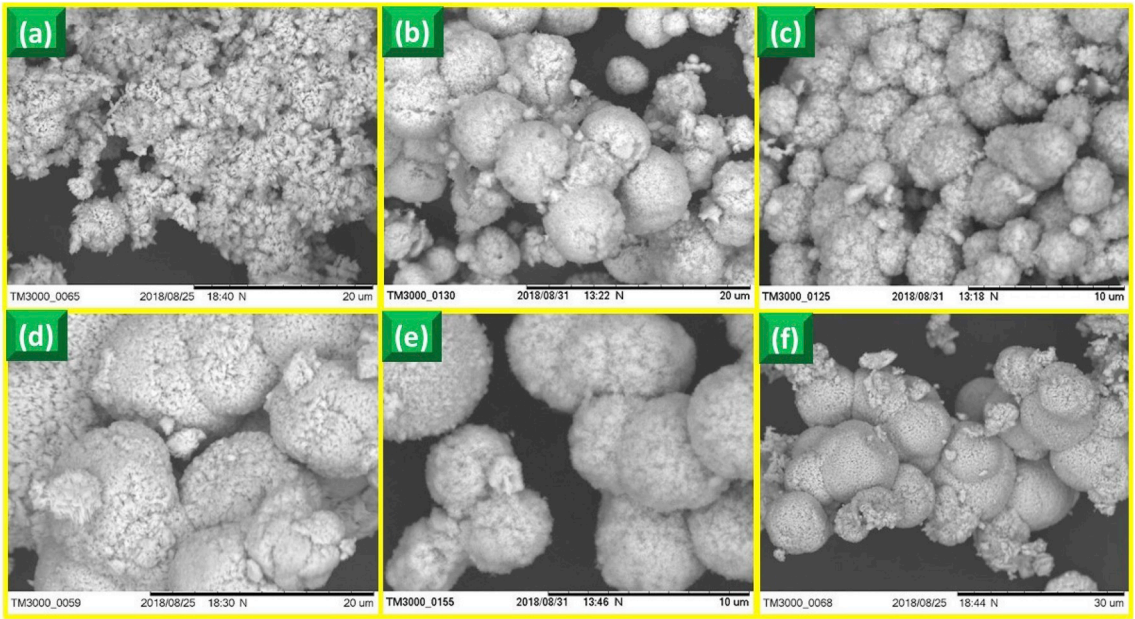

Fig. 5. SEM images of $Bi_2Zr_2O_7:Er^{3+}$ (5 mol %) NPs synthesized with different reaction time (12, 24, 36, 48, 60 and 72 h) by fixed *A.V.* gel concentration (35 ml) and temperature (200 °C).

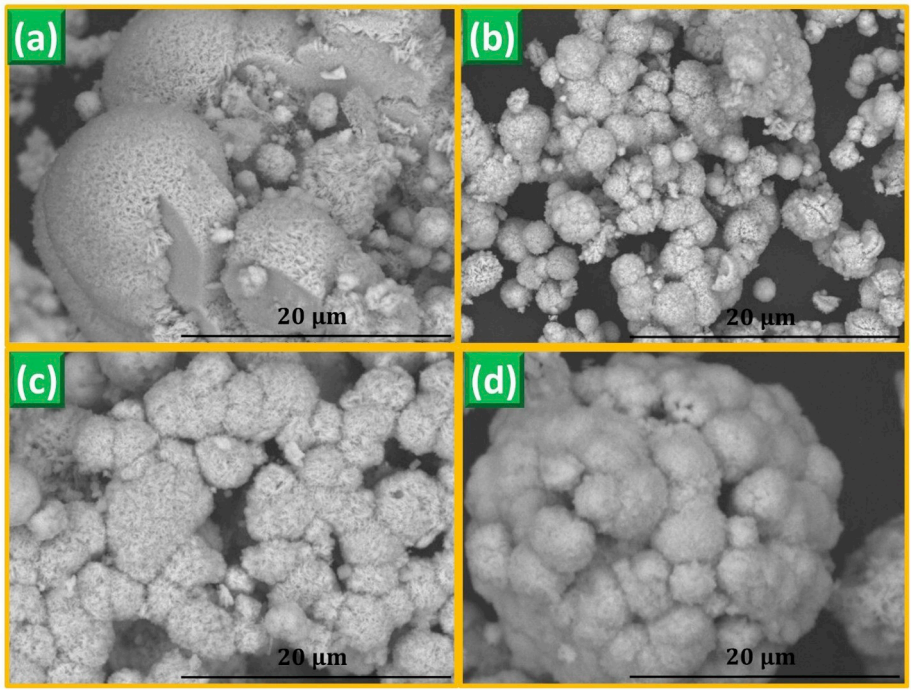

Fig. 6. SEM images of $Bi_2Zr_2O_7:Er^{3+}$ (5 mol %) NPs prepared by varying pH level (2, 5, 7 and 9) and fixed optimized hydrothermal parameters.

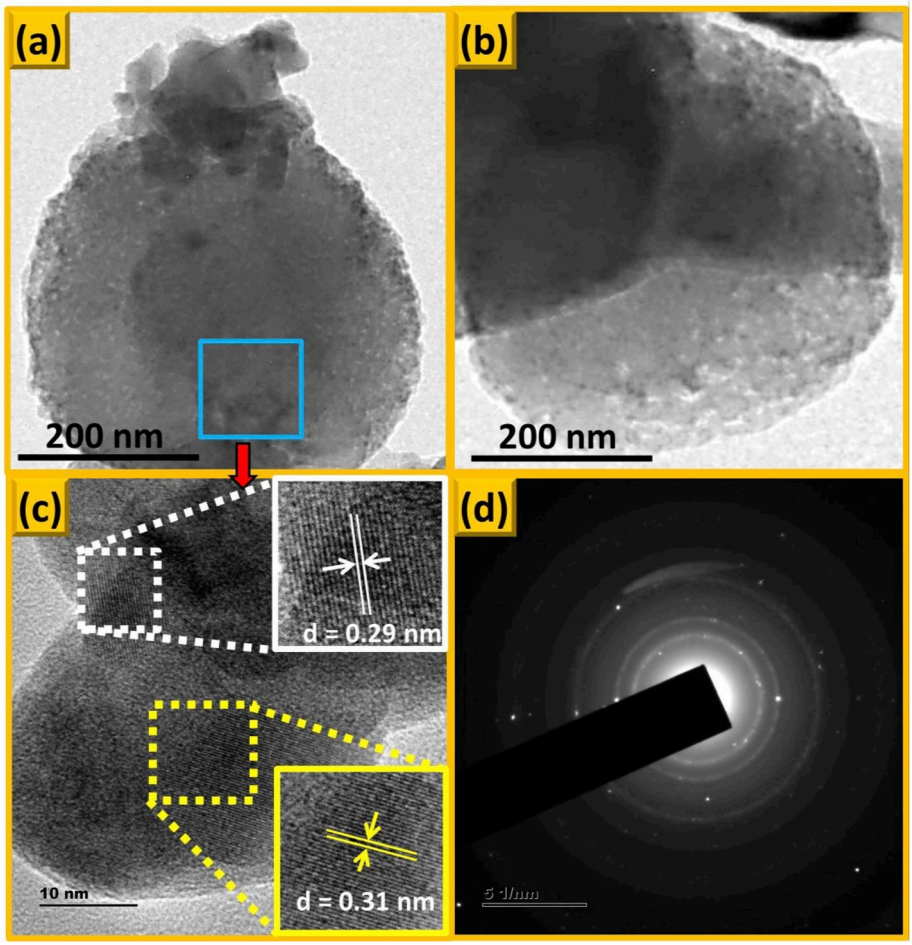

Fig. 7. (a, b) TEM images of $Bi_2Zr_2O_7:Er^{3+}$ (5 mol%) NPs prepared with fixed *A.V.* gel concentration (35 ml) and temperature (200 °C), (c) HRTEM and (d) SAED patterns of $Bi_2Zr_2O_7:Er^{3+}$ (5 mol %) NPs. [Inset of Fig. 9 (c) shows the enlarged portions of HRTEM image].

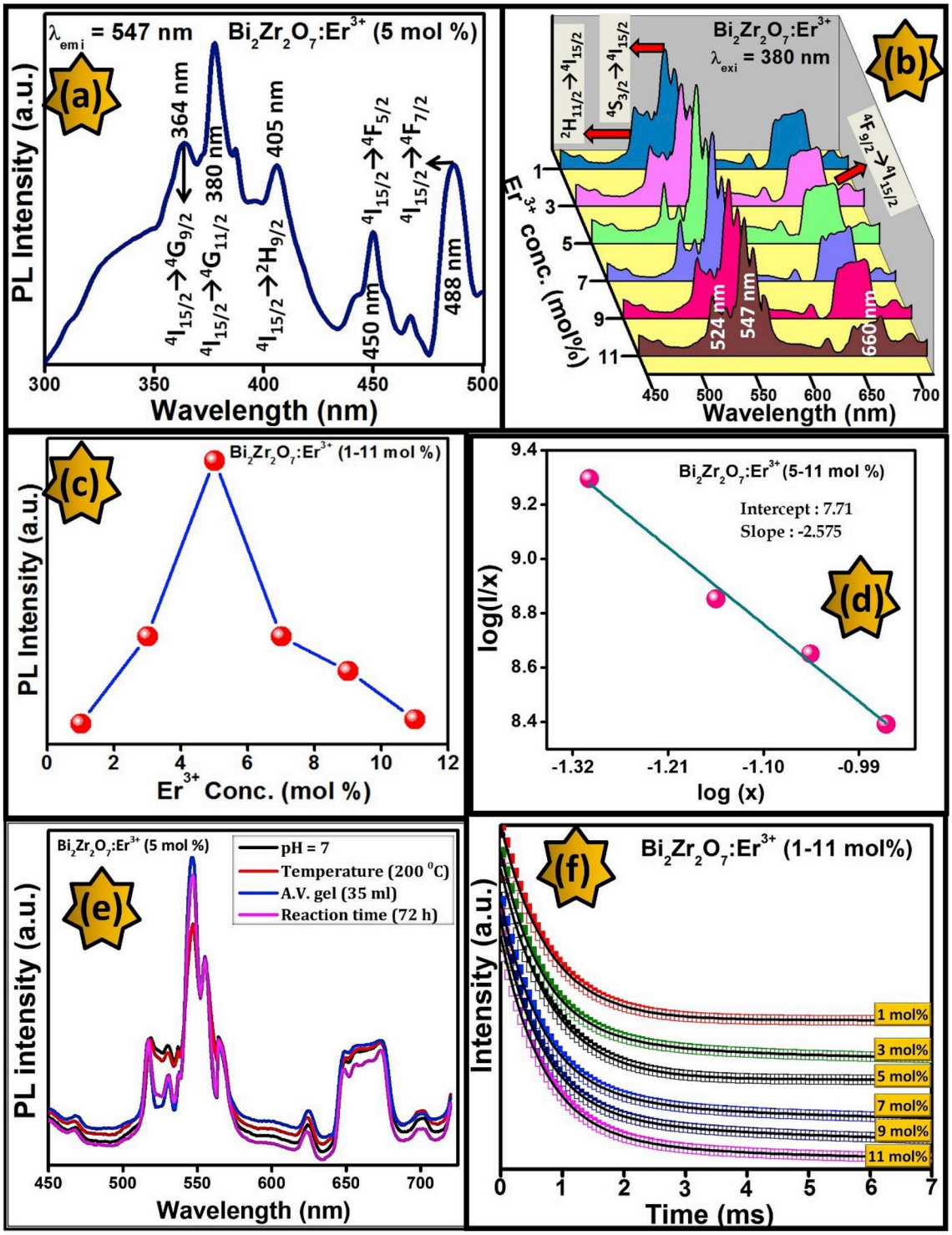

Fig. 8. (a) PL excitation spectrum of $Bi_2Zr_2O_7:Er^{3+}$ (5 mol %) NPs, (b) Emission spectra of $Bi_2Zr_2O_7:Er^{3+}$ (1–11 mol %) NPs excited at 380 nm wavelength, (c) Plot of PL intensity versus Er^{3+} concentration, (d) Logarithmic plot of (x) versus (I/x), (e) PL emission spectra of the $Bi_2Zr_2O_7:Er^{3+}$ (5 mol %) NPs synthesized by various optimized hydrothermal conditions and (f) PL decay profiles of $Bi_2Zr_2O_7:Er^{3+}$ (1–11 mol %) NPs.

$$R_c \approx 2\left[\frac{3V}{4X_c\pi Z}\right]^{1/3} \quad (3)$$

where, V; unit cell volume, X_c; critical Er^{3+} concentration and Z; number of cations in the unit cell. In the present study, V, X_c and Z were found to be ~450.31, 0.05 and 1, respectively. The value of R_c was estimated and found to be ~19.98 Å. The estimated R_c greater than 5 Å, indicates that the multipole–multipole interaction was dominant and was mainly responsible for concentration quenching. Generally, there are many types of multipolar interactions, namely dipole–dipole (d–d), dipole–quadrupole (d–q), quadrupole–quadrupole (q–q) interactions, and so on, which are involved in energy transfer. According to Dexter and Schulman theory, the emission intensity (I) per activator ion was given by [32];

$$\frac{I}{X} = k\left[1 + \beta(X)^{Q/3}\right]^{-1} \quad (4)$$

where k and β; constants, X; dopant concentration and Q; corresponding to exchange, d–d, d–q and q–q interactions are 6, 8 and 10, respectively. The plot of log (I/x) vs log(x) was shown in Fig. 8 (d). It was evident that, the plot was linear and slope was estimated to be −2.57. Therefore, the Q value was estimated and found to be ~7.71 (very close to theoretical value 8 for the electric d–q interaction), indicating that the dipole-quadrupole interaction was mainly responsible for concentration quenching. Further, the PL emission spectra of samples synthesized by various optimized hydrothermal conditions was studied and depicted in Fig. 8 (e). The spectra showed highest and lowest PL intensity was achieved for hydrothermally synthesized NPs using 35 ml A V. gel and pH 7, respectively.

The decay profiles of $Bi_2Zr_2O_7:Er^{3+}$ (1–11 mol %) NPs were shown in Fig. 8 (f). The decay profiles were well-fitted with bi-exponential relation [33];

$$I = A_1 \exp(-t/\tau_1) + A_2 \exp(-t/\tau_2) \quad (5)$$

where I_1, I_2 and τ_1, τ_2; corresponding PL intensities and time intervals, respectively. Further, the average lifetime (τ_{avg}) was also determined using relation;

$$\tau_{average} = \frac{I_1\tau_1^2 + I_2\tau_2^2}{I_1\tau_1 + I_2\tau_2} \quad (6)$$

The estimated average lifetime of $Bi_2Zr_2O_7:Er^{3+}$ (1–11 mol %) NPs were found to be in the range 1.85–1.95 ms.

The photometric characteristics of the prepared NPs were analyzed based on Commission Internationale de l'Eclairage (CIE) 1931 chromaticity coordinates and correlated color temperature (CCT) [34,35]. The CIE coordinates of optimized NPs were well located in the pure green region (0.368, 0.421) (Fig. 9 (a)). The CCT values were estimated based on the McCamy [36] empirical formula. CCT diagram of $Bi_2Zr_2O_7:Er^{3+}$ (1–11 mol %) NPs was shown in Fig. 9 (b). The average CCT value was found to be ~4611 K which was less than the 5000 K, indicating that the present phosphor was quite useful for the fabrication of warm light sources. The estimated CIE coordinates and CCT values were given in Table 3. In addition, color purity of the $Bi_2Zr_2O_7:Er^{3+}$ (1–11 mol %) NPs were estimated using the equation [37];

$$color\ \ purity = \frac{\sqrt{(x_s - x_i)^2 + (y_s - y_i)^2}}{\sqrt{(x_d - x_i)^2 + (y_d - y_i)^2}} \times 100\% \quad (7)$$

where (x_d, y_d); chromaticity coordinates of the dominant wavelength, (x_s, y_s); coordinates of coordinates of the sample point and (x_i, y_i); white illuminate (x_i = 0.33, y_i = 0.33). The color purity of $Bi_2Zr_2O_7:Er^{3+}$ (1–11 mol %) NPs were estimated and listed in Table 3.

3.2. Thermometric analysis

The temperature sensing ability of the $Bi_2Zr_2O_7:Er^{3+}$ (5 mol %) NPs were investigated by recording the temperature-dependent PL emission spectra with an excitation wavelength of ~380 nm, as shown in Fig. 10 (a). It was clearly evident that, the PL intensity of peaks at ~524 nm increases, whereas ~547 nm decreases with increase of temperature from 303 to 463 K without change in the emission bands. Therefore, their FIR values can also be affected by the temperature. Fluorescence intensity ratio (FIR) of two thermally coupled levels with respect to different temperatures was estimated using the Boltzmann distribution theory [38,39]:

$$FIR = \frac{I_H}{I_S} = A \exp\left(-\frac{\Delta E}{kT}\right) \quad (8)$$

where, I_H and I_S; integrated PL emission intensities corresponding to $^2H_{11/2} \rightarrow {}^4I_{15/2}$ (510–530 nm) and $^4S_{3/2} \rightarrow {}^4I_{15/2}$ (540–560 nm) transitions, A; constant, k; Boltzmann constant, ΔE; energy band gap between the $^2H_{11/2}$ and $^4S_{3/2}$ levels [40]. The estimated FIR values as a function of temperature was shown in Fig. 10 (b). By utilizing Eq. (8), the

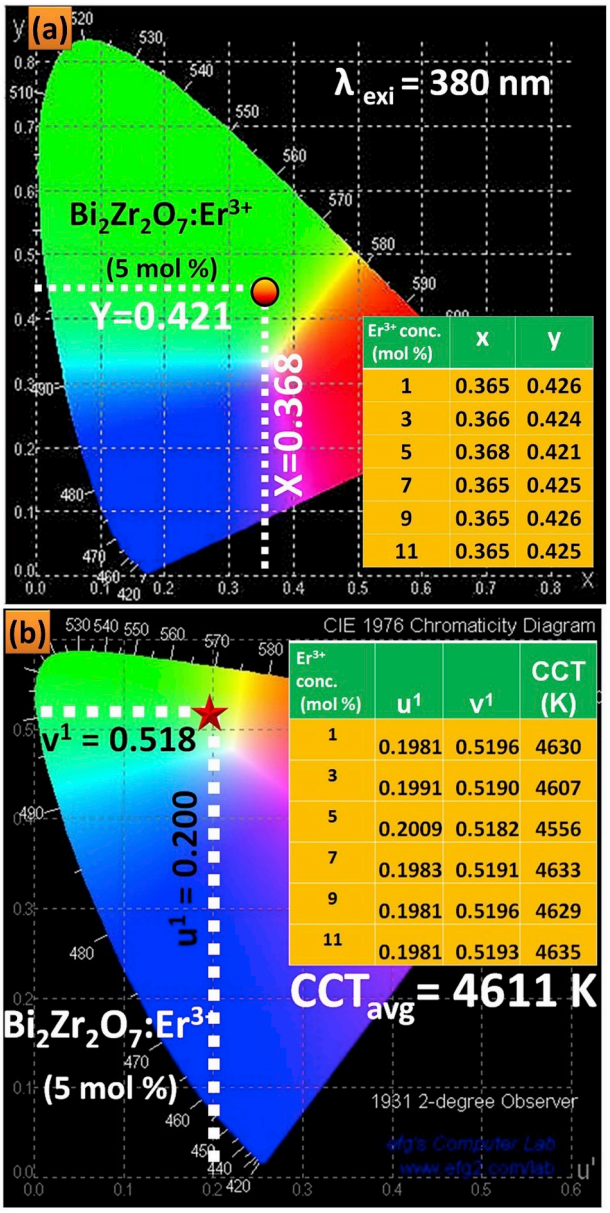

Fig. 9. (a) CIE and (b) CCT diagram of $Bi_2Zr_2O_7:Er^{3+}$ (1–11 mol %) NPs.

Table 3
Photometric parameters of $Bi_2Zr_2O_7:Er^{3+}$ (1–11 mol %) NPs.

Er^{3+} conc. (mol %)	CIE co-ordinates		CCT co-ordinates		CCT (K)	Color purity (%)
	X	Y	U^1	V^1		
1	0.365	0.426	0.191	0.519	4630	89
3	0.366	0.424	0.199	0.519	4607	90
5	0.368	0.421	0.200	0.518	4556	92
7	0.365	0.425	0.198	0.519	4633	91
9	0.365	0.426	0.198	0.519	4623	88
11	0.365	0.425	0.198	0.519	4635	91

experimental data was well fitted and the values of A and ΔE/k were found to be 48.6 and 1358.6, respectively. The above FIR expression can be rewritten as the form of the monolog plot of the FIR as a function of inverse temperature, as given below [41];

$$\ln(FIR) = -\frac{\Delta E}{kT} + B \quad (9)$$

where, B is a constant. Fig. 10 (c) depicts the plot of ln(FIR) as function

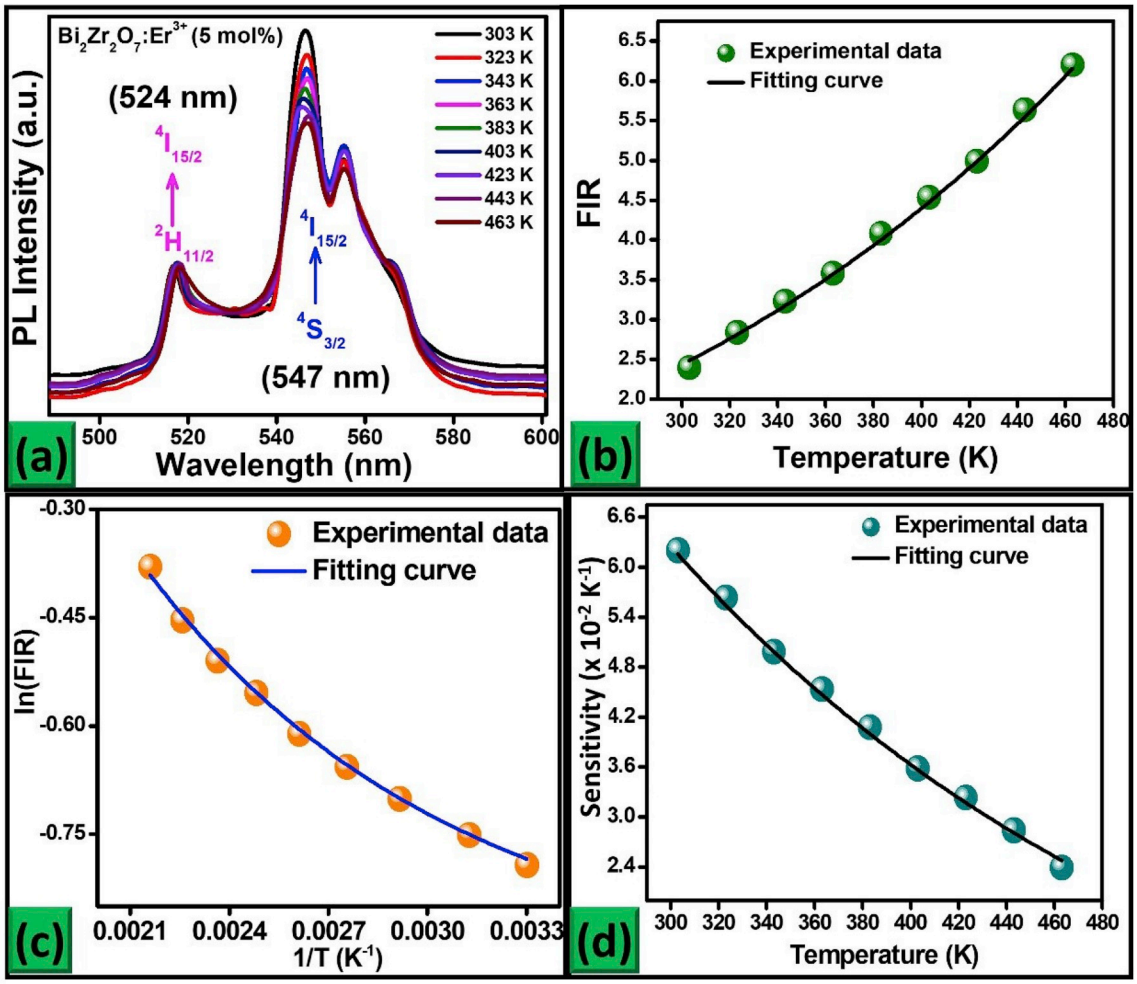

Fig. 10. (a) Temperature dependent PL spectra, (b) FIR values as a function of temperature, (c) Plot of ln(FIR) versus 1/T and (d) Sensor sensitivity as a function of temperature.

of inverse temperature. Evidently, the plot [ln(FIR) vs 1/T] was linear and slope and B value of the straight line was found to be −1273.9 and 4.2 respectively.

The temperature sensing behavior of the prepared $Bi_2Zr_2O_7:Er^{3+}$ (5 mol %) NPs was estimated by utilizing the following expression [42];

$$S = \frac{d(FIR)}{dT} = \left[A \exp\left(-\frac{\Delta E}{kT}\right)\right] X \frac{\Delta E}{kT^2} \quad (10)$$

The sensor sensitivity of $Bi_2Zr_2O_7:Er^{3+}$ (5 mol %) NPs as a function of temperature was obtained by fitting Eq. (10) and the corresponding result was depicted in Fig. 10 (d). It was evident from the figure that sensor sensitivity was mainly dependent on the temperature and its maximum value was found to be ~0.0621 K^{-1} when the temperature was 303 K. The obtained sensor sensitivity of the $Bi_2Zr_2O_7:Er^{3+}$ (5 mol %) NPs were much higher as compared to previous literature [43–48], as listed in Table 4. Aforementioned results confirm that the optimized NPs was considered to be the most promising candidate for optical thermometry applications.

3.3. Thermoluminescence studies

Fig. 11 (a) shows the TL glow curves of $Bi_2Zr_2O_7$: Er^{3+} (1–11 mol %) NPs recorded at a γ-dose of 1 kGy. It was evident from the figure that, all the TL curves exhibit similar TL glow curves with a slight variation in glow peak temperature. In addition, variation of TL intensity of $Bi_2Zr_2O_7$: Er^{3+} (1–11 mol %) NPs under exposure of γ-ray dose of 1 kGy was shown in the inset of Fig. 11 (a). It was evident that, the TL

Table 4
Sensor sensitivities and ΔE/k values of Er3+- doped temperature sensing materials.

Materials	ΔE/k	S_{max} (K^{-1})	References
$Sr_{0.69}La_{0.31}F_{2.31}:Er^{3+}$	904.98	0.0101	Wang et al. [43]
$Na_5Gd_9F_{32}:Er^{3+}$	998.60	0.0110	Li et al. [44]
$NaYb_2F_7:Er^{3+}$	1226.40	0.0136	Hu et al. [45]
$YNbO_4:Er^{3+}/Yb^{3+}$	759.60	0.0085	Tian et al. [46]
BiF_3: Er^{3+}/Yb^{3+}	1280.68	0.0151	Du et al. [47]
$Gd_2(MoO_4)_3$: Er^{3+}/Yb^{3+}	1168.00	0.0134	Lu et al. [48]
$Bi_2Zr_2O_7:Er^{3+}$	1149.50	0.0621	Present work

intensity gradually increases with increase of Er^{3+} ion concentration up to 5 mol % and later diminishes. This decrement in the TL intensity with increasing of Er^{3+} ion concentration was mainly due to concentration quenching. The doping of Er^{3+} ions into $Bi_2Zr_2O_7$ site results creation of defect levels between the conduction and valence bands. After γ-irradiation, the population of defects also increased due to source energy. As the Er^{3+} ions concentration increases, the number of defect levels between the bands increases [49]. The number of defects exceeds a certain limit, overlapping of defect centre takes place, which has no contribution to the additional TL output and renowned as concentration quenching.

Further, the TL curves of $Bi_2Zr_2O_7$: Er^{3+} (5 mol %) NPs irradiated with various γ-ray dose (1–6 kGy) was shown in Fig. 11 (b). It was noticed that, TL curve intensity was found to increase linearly up to a

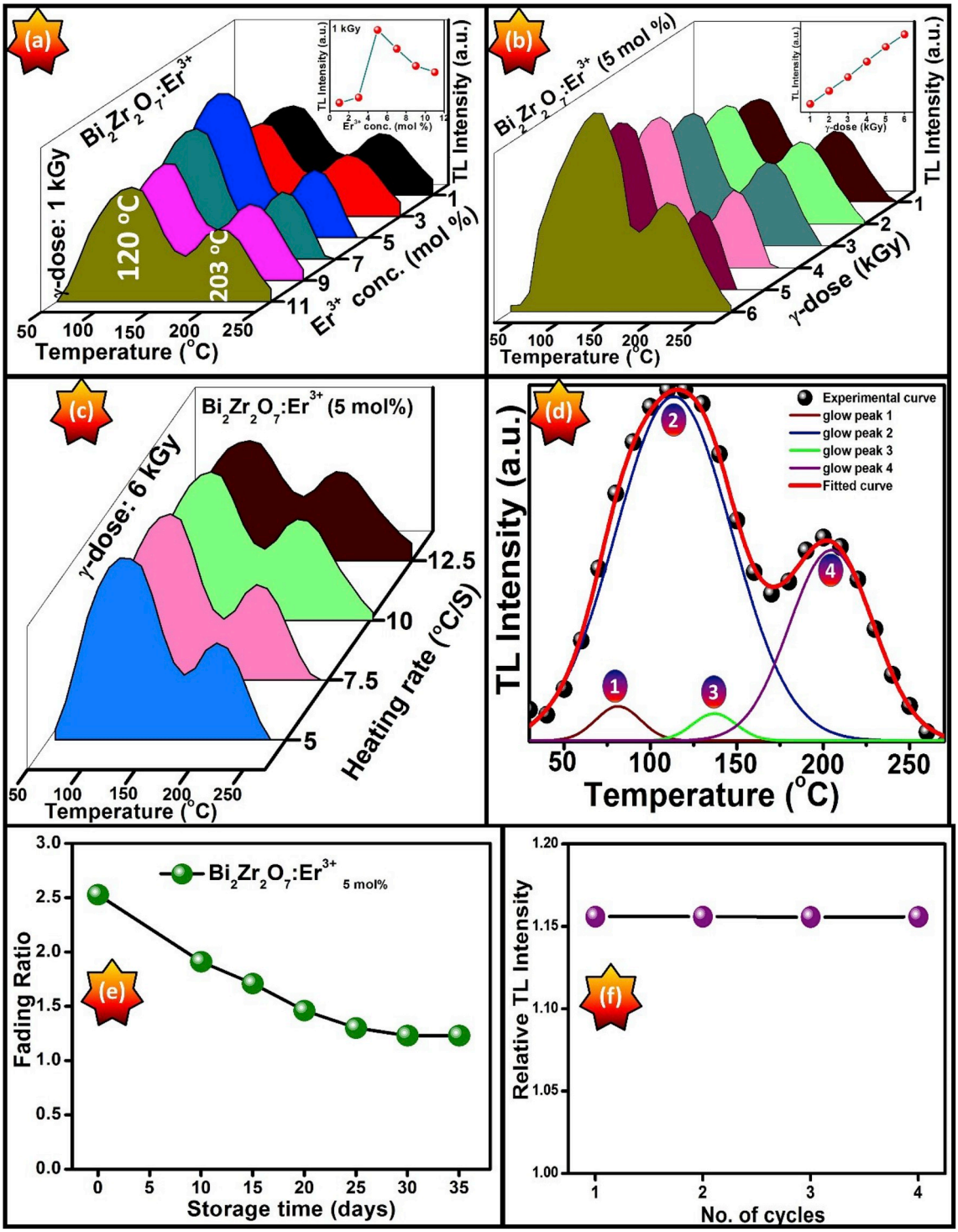

Fig. 11. (a) TL glow curves of $Bi_2Zr_2O_7:Er^{3+}$ (1–11 mol %) NPs at a γ-dose of 1 kGy [Inset: Variation of intensity of TL glow peak as a function of Er^{3+} concentration], (b) TL glow curves of $Bi_2Zr_2O_7:Er^{3+}$ (5 mol %) NPs with different γ-dose irradiation (1–6 kGy) [Inset: Intensity of TL glow curves versus γ-dose], (c) TL glow curves of $Bi_2Zr_2O_7$: Er^{3+} (5 mol %) NPs irradiated with 6 kGy γ-dose at the various heating rates (5, 7.5, 10 and 12.5 °C/s), (d) Deconvoluted peaks of $Bi_2Zr_2O_7:Er^{3+}$ (5 mol %) NPs with 6 kGy γ-dose, (e) Plot of fading ratio versus storage time and (f) reproducibility plot.

given γ-dose, indicating that the phosphor was quite useful for dosimetric applications. The linear increase in TL intensity with γ-dose (Inset of Fig. 11 (b)) was mainly due to the interaction among γ-rays and NPs. In general, (i) photoelectric effect, (ii) Compton effect and (iii) pair production are the main reasons for explaining the interaction between γ-rays with NPs [50]. In the present work, the interaction with Compton effect and photoelectric effect was more when compared to pair production due to significant energy of ^{60}Co source. Fig. 11 (c) shows the TL glow curves of $Bi_2Zr_2O_7$: Er^{3+} (5 mol %) NPs irradiated with 6 kGy γ-dose at the various heating rates (5, 7.5, 10 and 12.5 °C/s). A small shift of the prominent TL glow peak towards the high temperature region was observed with the increase of the heating rate. This increment in the peak intensity with respect to heating rate, suggesting the exclusion of thermal quenching which was fundamentally required for TL dosimetric applications [51]. The various trapping parameters were calculated by using TL glow curves of $Bi_2Zr_2O_7$: Er^{3+} (5 mol %)

Table 5
Summary of the activation energy (E) values, shape factor (μ), frequency factor (S) and average energy of the glow curve of $Bi_2Zr_2O_7:Er^{3+}$ (5 mol %) NPs irradiated with different γ-doses of the.

γ-dose (KGy)	Glow Peak	T_m (°C)	b (μ_g)	Activation energy, E (eV)				Frequency factor (s) (Hz)
				E_τ	E_δ	E_ω	E_{ave}	
1	1	76	2(0.83)	0.232	0.223	0.446	0.761	2.8E + 09
	2	120	2(0.51)	0.136	0.311	0.262	0.941	1.2E + 09
	3	148	2(0.53)	0.138	0.313	0.278	0.945	1.6E + 09
	4	203	2(0.52)	0.154	0.136	0.294	1.336	3.1E + 09
2	1	76	2(0.49)	0.163	0.163	0.321	0.754	2.2E + 10
	2	120	2(0.51)	0.208	0.214	0.432	0.694	1.6E + 08
	3	148	2(0.53)	0.137	0.312	0.279	0.944	1.6E + 09
	4	203	2(0.47)	0.197	0.196	0.391	1.577	4.1E + 08
3	1	76	2(0.51)	0.238	0.214	0.454	0.616	2.4E + 17
	2	120	2(0.50)	0.119	0.132	0.571	0.574	2.6E + 06
	3	148	2(0.52)	0.138	0.313	0.281	0.946	1.6E + 09
	4	203	2(0.53)	0.132	0.125	0.244	1.441	8.8E + 09
4	1	76	2(0.49)	0.231	0.226	0.254	1.031	3.4E + 10
	2	120	2(0.51)	0.126	0.113	0.453	1.394	5.4E + 13
	3	148	2(0.51)	0.139	0.312	0.283	0.945	1.6E + 09
	4	203	2(0.52)	0.296	0.254	0.547	1.633	1.1E + 09
5	1	76	2(0.51)	0.744	0.144	0.144	0.651	7.3E + 11
	2	120	2(0.50)	0.167	0.164	0.337	1.024	2.8E + 09
	3	148	2(0.51)	0.140	0.314	0.283	0.945	1.6E + 09
	4	203	2(0.50)	0.273	0.281	0.554	1.488	8.5E + 19
6	1	76	2(0.52)	0.738	0.144	0.144	0.657	7.2E + 11
	2	120	2(0.48)	0.157	0.163	0.336	1.026	2.7E + 09
	3	148	2(0.51)	0.139	0.312	0.284	0.948	1.6E + 09
	4	203	2(0.51)	0.276	0.281	0.551	1.487	8.5E + 09

NPs irradiated with 6 kGy γ-dose data, as described in the reported literature. The combined experimental and deconvoluted TL glow curves of $Bi_2Zr_2O_7:Er^{3+}$ (5 mol %) NPs irradiated with 6 kGy γ-dose data were shown in Fig. 11 (d). The deconvoluted TL glow curves exhibit four distinct peaks at ~60, 110, 140 and 205 °C.

The quality of the fitted glow curves was estimated by calculating the parameter called Figure of Merit (FOM), as given below [52];

$$FOM = \frac{\sum TL_{Exp} - TL_{The}}{\sum TL_{The}} \quad (11)$$

where, TL_{Exp} and TL_{The}; TL intensity of experimental and theoretically obtained glow curves, respectively. In the present study, the FOM values of $Bi_2Zr_2O_7:Er^{3+}$ (5 mol %) NPs irradiated with 6 kGy γ-dose were estimated and found to be 1.64%. The estimated values were found to be < 5%, indicating that a good agreement among the experimental and theoretically obtained results. The estimated trapping parameters of $Bi_2Zr_2O_7:Er^{3+}$ (5 mol %) NPs irradiated with various γ-ray dose (1–6 kGy) are listed in Table 5.

Fig. 11 (e) shows the TL stability of the prominent glow peak (120 °C) of $Bi_2Zr_2O_7:Er^{3+}$ (5 mol %) NPs exposed to 6 KGy γ-irradiation with different time periods. As can be evident from the figure that, the 120 °C glow peak fade 25% for the first 20 days of storage and thereafter the fading was gradual. Further, with increase of storage time up to 35 days, 45% fading was noticed. This was high enough for the present material useful in dosimetric applications [53–55]. In addition to this, the reusability of the prepared $Bi_2Zr_2O_7:Er^{3+}$ (5 mol %) NPs after many reiterations of exposures and readouts was studied. Initially, the TL glow curves of optimized NPs exposed to 6 KGy γ-irradiation were recorded from room temperature to 300 °C. After that, the NPs was quickly cooled to room temperature and again irradiated with same γ-dose and its corresponding glow curve was recorded. The experiment was performed by such repeated cycles of exposures and readouts and its glow curve was recorded. The results after four repeated cycles of annealing-irradiation-readout was shown in Fig. 11 (f). As evident from the figure that, the slight variation in the TL intensity peak during four cycles of readout, which obviously specify that $Bi_2Zr_2O_7:Er^{3+}$ (5 mol %) NPs can be reused for many times to record the absorbed amount of radiation in radiation rich areas.

4. Conclusions

Novel $Bi_2Zr_2O_7:Er^{3+}$ (1–11 mol %) NPs were fabricated by simple hydrothermal route. Morphology of the sample was highly dependent on various hydrothermal conditions. The energy band gap values are estimated and found to be in the range of 2.63–2.67 eV. The PL emission spectra shows intense peaks at ~524, 547 and 660 nm attributed to $^2H_{11/2} \rightarrow {}^4I_{15/2}$, $^4S_{3/2} \rightarrow {}^4I_{15/2}$ and $^4F_{9/2} \rightarrow {}^4I_{15/2}$ intra 4–4f transitions of Er^{3+} ions, respectively. The sensor sensitivity of the $Bi_2Zr_2O_7:Er^{3+}$ (5 mol %) NPs was found to be ~0.0621 K^{-1} at lower temperature 282 K, suggesting suitability for the optical thermometry application. The CIE co-ordinates are located in the green region and the average CCT was found to be ~4611 K, which was less than 5000 K indicates that the phosphor was a potentially active component in warm LEDs. The TL glow curves of samples irradiated with γ-rays showed two peaks at ~120 and 203 °C. Up to a given dose, the TL intensity at 120 °C peak was found to increase linearly. The optimized sample showed the simple glow curve structure with less fading and good reusability. The aforementioned results clearly indicate that the optimized NPs was quite useful for multi-functional applications.

Declaration of interests

The authors declare that they have no known competing financial interests or personal relationships that could have appeared to influence the work reported in this paper.

References

[1] S.K. Chaudhuri, L. Malodia, Biosynthesis of zinc oxide nanoparticles using leaf extract of *Calotropis gigantea*: characterization and its evaluation on tree seedling growth in nursery stage, Appl. Nanosci. 7 (2017) 501–512.
[2] R.G. Saratale, I. Karuppusamy, G.D. Saratale, A. Pugazhendhi, G. Kumar, Y. Park, G.S. Ghodake, R.N. Bhargava, J.R. Banu, H.S. Shin, A comprehensive review on green nanomaterials using biological systems: recent perception and their future applications, Colloids Surf., B: Bio 170 (2018) 20–35.
[3] M. Oves, M. Aslam, M.A. Rauf, S. Qayyum, H.A. Qari, M.S. Khan, M.Z. Alam, S. Tabrez, A. Pugazhendhi, I.M. Ismail, Antimicrobial and anticancer activities of

silver nanoparticles synthesized from the root hair extract of Phoenix dactylifera, Mater. Sci. Eng. C 89 (2018) 429–443.
[4] Arivalagan Pugazhendhi, Raju Prabhu, Kavitha Muruganantham, Rajasree Shanmuganathan, Suganthy Natarajan, Anticancer, antimicrobial and photocatalytic activities of green synthesized magnesium oxide nanoparticles (MgONPs) using aqueous extract of *Sargassum wightii*, J. Photochem. Photobiol. B Biol. 190 (2019) 86–97.
[5] V. Makarov, A. Love, O. Sinitsyna, S. Makarova, I. Yaminsky, M. Taliansky, N. Kalinina, Green nanotechnologies: synthesis of metal nanoparticles using plants, Acta Naturae 6 (2014).
[6] D. Gupta, B. Bleakley, R.K. Gupta, Dragon's blood: botany, chemistry and therapeutic uses, J. Ethnopharmacol. 115 (2008) 361–380.
[7] S. Ling, L. Nheu, A. Dai, Z. Guo, P. Komesaroff, Effects of four medicinal herbs on human vascular endothelial cells in culture, Int. J. Cardiol. 128 (2008) 350–358.
[8] P. Logeswari, S. Silambarasan, J. Abraham, Synthesis of silver nanoparticles using plants extract and analysis of their antimicrobial property, J. Saudi Chem. Soc. 19 (2015) 311–317.
[9] G.P. Darshan, H.B. Premkumar, H. Nagabhushana, S.C. Sharma, B. Daruka Prasad, S.C. Prashantha, R.B. Basavaraj, Superstructures of doped yttrium aluminates for luminescent and advanced forensic investigations, J. Alloy. Comp. 686 (2016) 577–587.
[10] M. Dhanalakshmi, R.B. Basavaraj, G.P. Darshan, S.C. Sharma, H. Nagabhushana, Pivotal role of fluxes in $BaTiO_3$:Eu^{3+} nano probes for visualization of latent fingerprints on multifaceted substrates and anti-counterfeiting applications, Microchem. J. 145 (2019) 226–234.
[11] K.N. Venkatachalaiah, H. Nagabhushana, G.P. Darshan, R.B. Basavaraj, B. Daruka Prasad, S.C. Sharma, Structural, morphological and photometric properties of sonochemically synthesized Eu^{3+} doped Y_2O_3 nanophosphor for optoelectronic devices, Mater. Res. Bull. 94 (2017) 442–455.
[12] G.P. Darshan, H.B. Premkumar, H. Nagabhushana, S.C. Sharma, S.C. Prashantha, H.P. Nagaswarupa, B. Daruka Prasad, Blue light emitting ceramic nano-pigments of Tm^{3+} doped $YAlO_3$: applications in latent finger print, anti-counterfeiting and porcelain stoneware, Dyes Pigments 131 (2016) 268–281.
[13] K.N. Venkatachalaiah, H. Nagabhushana, G.P. Darshan, R.B. Basavaraj, B. Daruka Prasad, Novel and highly efficient red luminescent sensor based SiO_2@Y_2O_3:Eu^{3+}, M^+ (M^+ = Li, Na, K) composite core–shell fluorescent markers for latent fingerprint recognition, security ink and solid state lightning applications, Sens. Actuators, B 251 (2017) 310–325.
[14] R. B Basavaraj, H. Nagabhushana, G.P. Darshan, B. Daruka Prasad, S.C. Sharma, K.N. Venkatachalaiah, Ultrasound assisted rare earth doped Wollastonite nanopowders: labeling agent for imaging eccrine latent fingerprints and cheiloscopy applications, J. Ind. Eng. Chem. 51 (2017) 90–105.
[15] H.S. Yogananda, R.B. Basavaraj, G.P. Darshan, B. Daruka Prasad, Ramachandra Naik, S.C. Sharma, H. Nagabhushana, New design of highly sensitive and selective MoO_3:Eu^{3+} micro-rods: probing of latent fingerprints visualization and anti-counterfeiting applications, J. Colloid Interface Sci. 528 (2018) 443–456.
[16] Asha Panghal, Pawan K. Kulriya, Yogendra Kumar, Fouran Singh, N.L. Singh, Investigations of atomic disorder and grain growth kinetics in polycrystalline $La_2Zr_2O_7$, Appl. Phys. A 125 (2019) 428.
[17] Yijia Luo, Liyun Cao, Liangliang Feng, Jianfeng Huang, Liuqing Yang, Chunyan Yao, Yayi Cheng, Synthesis, characterization and photocatalytic properties of nanoscale pyrochlore type $Bi_2Zr_2O_7$, Mater. Sci. Eng., B 240 (2019) 133–139.
[18] Yijia Luo, Liyun Cao, Jianfeng Huang, Liangliang Feng, Chunyan Yao, A new approach to preparing $Bi_2Zr_2O_7$ photocatalysts for dye degradation, Mater. Res. Express 5 (2018) 1.
[19] Xiaowei Liu, Lihui Huang, Xueyuan Wu, Zexiang Wang, Guihua Dong, Chuang Wang, Yangyang Liu, Lisha Wang, $Bi_2Zr_2O_7$ nanoparticles synthesized by soft-templated sol-gel methods for visible-light-driven catalytic degradation of tetracycline, Chemosphere 210 (2018) 424–432.
[20] Tingting He, Deyong Wu, Yuanbing Tan, Haiyan Tan, Ag/AgI modified $Bi_2Zr_2O_7$ nanosheets with excellent photocatalytic activity, Mater. Lett. 193 (2017) 210–212.
[21] Tingting He, Deyong Wu, Synthesis and characterization of Ag/AgCl/$Bi_2Zr_2O_7$ photocatalyst with enhanced visible-light-driven photocatalytic performance, J. Mater. Sci. Mater. Electron. 28 (2017) 7320–7325.
[22] Deyong Wu, Tingting He, Xia Jin, Yuanbin Tan, Preparation and photocatalytic properties of $Bi_2Zr_2O_7$ photocatalyst, Mater. Lett. 156 (2015) 195–197.
[23] Vaishali M. Sharma, Dipankar Saha, Giridhar Madras, T.N. Guru Row, Synthesis, structure, characterization and photocatalytic activity of $Bi_2Zr_2O_7$ under solar radiation, RSC Adv. 3 (2013) 18938–18943.
[24] M. Venkataravanappa, H. Nagabhushana, B. Daruka Prasad, G.P. Darshan, R.B. Basavaraj, G.R. Vijayakumar, Dual colour emitting Eu doped strontium orthosilicate phosphors synthesized by bio-template assisted ultrasound for solid state lightning and display applications, Ultrason. Sonochem. 34 (2017) 803–820.
[25] G.P. Darshan, H.B. Premkumar, H. Nagabhushana, S.C. Sharma, S.C. Prashantha, B. Daruka Prasad, Effective fingerprint recognition technique using doped yttrium aluminate nano phosphor material, J. Colloid Interface Sci. 464 (2016) 206–218.
[26] R.B. Basavaraj, H. Nagabhushana, G.P. Darshan, B. Daruka Prasad, M. Rahul, S.C. Sharma, R. Sudaramani, K.V. Archana, Red and green emitting CTAB assisted $CdSiO_3$:Tb^{3+}/Eu^{3+} nanopowders as fluorescent labeling agents used in forensic and display applications, Dyes Pigments 147 (2017) 364–377.
[27] Lakshmi Mukhopadhyaya, Vineet Kumar Rai, Upconversion based near white light emission, intrinsic optical bistability and temperature sensing in Er^{3+}/Tm^{3+}/Yb^{3+}/Li^+:$NaZnPO_4$ phosphors, New J. Chem. 41 (2017) 7650–7661.
[28] G.P. Darshan, H.B. Premkumar, H. Nagabhushana, S.C. Sharma, B. Daruka Prasad, S.C., Prashantha Neodymium doped yttrium aluminate synthesis and optical properties - a blue light emitting nanophosphor and its use in advanced forensic analysis, Dyes Pigments 134 (2016) 227–233.
[29] M. Mangalagowri, R.B. Basavaraj, G.P. Darshan, M.S. Raju, Yashwanth V. Naik, D. Kavyashree, Hajeebaba K. Inamdar, S.C. Sharma, H. Nagabhushana, Sonochemical synthesis of green emitting Ca_2SiO_4:Er^{3+} nanopowders: promising applications in optical thermometry and radiation dosimeter, Opt. Mater. 92 (2019) 125–135.
[30] R. Mohan P, S. Gopi, V. Vidyadharan, A. George, C. Joseph, N.V. Unnikrishnan, P.R. Biju, Synthesis and luminescence characteristics of CaB_2O_4:Er^{3+}, Li^+ phosphor, J. Lumin. 187 (2017) 113–120.
[31] M. Venkataravanappa, H. Nagabhushana, G.P. Darshan, B. Daruka Prasad, G.R. Vijayakumar, H.B. Premkumar, Udayabhanu, Novel EGCG assisted ultrasound synthesis of self-assembled Ca_2SiO_4:Eu^{3+} hierarchical superstructures: photometric characteristics and LED applications, Ultrason. Sonochem. 33 (2016) 226–239.
[32] G.P. Darshan, H.B. Premkumar, H. Nagabhushana, S.C. Sharma, B. Umesh, R.B. Basavaraj, Nucleation and self-assembly dynamics of hierarchical $YAlO_3$:Ce^{3+} architectures: nano probe for in vitro dermatoglyphics and anti-mimetic applications, Mater. Sci. Eng. C 99 (2019) 282–295.
[33] F. Femila Komahal, H. Nagabhushana, R.B. Basavaraj, G.P. Darshan, B. Daruka Prasad, Solvothermal synthesis and luminescent properties of hierarchical flower-like $ZnAl_2O_4$:Ho^{3+} microstructures, Opt. Mater. 84 (2018) 536–544.
[34] Xiangfu Wang, Ye Wang, Leisheng Jin, Yanyan Bu, X.L. Yang, Xiaohong Yan, Controlling optical temperature detection of $Ca_3Al_2O_6$: Yb^{3+}, Er^{3+} phosphors through doping, J. Alloy. Comp. 773 (2019) 393–400.
[35] N.H. Deepthi, G.P. Darshan, R.B. Basavaraj, B. Daruka Prasad, H. Nagabhushana, Large-scale controlled bio-inspired fabrication of 3D CeO_2:Eu^{3+} hierarchical structures for evaluation of highly sensitive visualization of latent fingerprints, Sens. Actuators, B 255 (2018) 3127–3147.
[36] H.S. Sudheendra, G.P. Darshan, R.B. Basavaraj, Yashwanth V. Naik, H.B. Premakumar, H. Nagabhushana, J.F. Williams, K. Hareesh, M.K. Kokila, Influence of Zn^{2+} doping on the lattice defects and photoluminescence studies of Sr_2CeO_4:Eu^{3+} nanophosphor: applications for data encryption strategies, Opt. Mater. 90 (2019) 159–171.
[37] C.J. Shilpa, R.B. Basavaraj, G.P. Darshan, H.B. Premkumar, S.C. Sharma, H. Nagabhushana, New insights into the rapid deposition and visualization of latent fingerprints: cyan light emitting $GdAlO_3$:Ce^{3+} nano fluorescent probe, J. Photochem. Photobiol. A Chem. 376 (2019) 288–304.
[38] J. Zhong, D. Chen, Y. Peng, Y. Lu, X. Chen, X. Li, Z. Ji, A review on nanostructured glass ceramics for promising application in optical thermometry, J. Alloy. Comp. 763 (2018) 34–48.
[39] P. Du, L. Luo, X. Huang, J.S. Yu, Ultrafast synthesis of bifunctional Er^{3+}/Yb^{3+}-codoped $NaBiF_4$ upconverting nanoparticles for nanothermometer and optical heater, J. Colloid Interface Sci. 514 (2018) 172–181.
[40] Hang Liu, Chenbin Zuo, Yunhe Liu, Gui Gao, Dan Liu, Tingting Wang, Tianyu Liu, Yuhong Zhang, Optical thermometry through infrared excited green upconversion of $KLa(MoO_4)_2$:Yb^{3+}/Er^{3+} phosphor, J. Lumin. 207 (2019) 93–97.
[41] A. Maurya, A. Bahadur, A. Dwivedi, A.K. Choudhary, T.P. Yadav, P.K. Vishwakarma, S.B. Rai, Optical properties of Er^{3+}, Yb^{3+} co-doped calcium zirconate phosphor and temperature sensing efficiency: effect of alkali ions (Li^+, Na^+ and K^+), J. Phys. Chem. Solids 119 (2018) 228–237.
[42] X. Li, J. Cao, F. Hu, R. Wei, H. Guo, Transparent $Na_5Gd_9F_{32}$:Er^{3+} glass-ceramics: enhanced up-conversion luminescence and applications in optical temperature sensors, RSC Adv. 7 (2017) 35147–35153.
[43] X. Wang, Q. Liu, P. Cai, J. Wang, L. Qin, T. Vu, H.J. Seo, Excitation powder dependent optical temperature behavior of Er^{3+} doped transparent $Sr_{0.69}La_{0.31}F_{2.31}$ glass ceramics, Optic Express 24 (2016) 17792–17804.
[44] X. Li, J. Cao, F. Hu, R. Wei, H. Guo, Transparent $Na_5Gd_9F_{32}$:Er^{3+} glass-ceramics: enhanced up-conversion luminescence and applications in optical temperature sensors, RSC Adv. 7 (2017) 35147–35153.
[45] F. Hu, J. Cao, X. Wei, X. Li, J. Cai, H. Guo, Y. Chen, C. Duan, M. Yin, Luminescence properties of Er^{3+}-doped transparent $NaYb_2F_7$ glass-ceramics for optical thermometry and spectral conversion, J. Mater. Chem. C 4 (2016) 9976–9985.
[46] Y. Tian, Y. Tian, P. Huang, L. Wang, Q. Shi, C. Cui, Effect of Yb^{3+} concentration on upconversion luminescence and temperature sensing behavior in Yb^{3+}/Er^{3+} co-doped $YNbO_4$ nanoparticles prepared via molten salt route, Chem. Eng. J. 297 (2016) 26–34.
[47] P. Du, J.S. Yu, Synthesis of Er(III)/Yb(III)-doped BiF_3 upconversion nanoparticles for use in optical thermometry, Microchim. Acta 185 (2018) 237.
[48] H. Lu, H. Hao, Y. Gao, G. Shi, Q. Fan, Y. Song, Y. Wang, X. Zhang, Dual functions of Er^{3+}/Yb^{3+} codoped $Gd_2(MoO_4)_3$ phosphor: temperature sensor and optical heater, J. Lumin. 191 (2017) 13–17.
[49] Jyoti Singh, J. Manam, Fouran Singh, Synthesis and thermoluminescence studies of γ-irradiated Dy^{3+} doped $SrGd_2O_4$ phosphor, Mater. Res. Bull. 94 (2017) 113–121.
[50] Mehdi Souli, Yassine Bensalem, Mihail Secu, Cristina Barthab, Monica Enculescu, Arbi Mejri, Najoua Kamoun-Turki, Petre Badica, Effect of high gamma radiations on physical properties of In_2S_3 thin films grown by chemical bath deposition for buffer layer applications, Results Phys. 13 (2019) 102115.
[51] Jyoti Singh, J. Manam, Fouran Singh, Thermoluminescence studies of solid-state reaction derived and g-irradiated $SrGd_2O_4$: Eu^{3+} phosphor, Mater. Res. Bull. 93 (2017) 318–324.
[52] Dewangan Pradeep, D.P. Bisen, Nameeta Brahme, Shweta Sharma, Structural characterization and luminescence properties of Dy^{3+} doped $Ca_3MgSi_2O_8$ phosphors, J. Alloy. Comp. 777 (2019) 423–433.
[53] Arun Kumar, Arvind Kumar, Rakesh Dogra, Mohit Manhas, Sandeep Sharma, Ravi Kumar, Investigation of thermoluminescence and kinetic parameters of gamma ray exposed LiF: Sm^{3+}, Eu^{3+} nanophosphors for dosimetric applications, Ceram. Int. 44 (2018) 15535–15541.
[54] S. Delice, M. Isik, N.M. Gasanly, Characterization of trap centers in Gd_2O_3 nanoparticles by low temperature thermoluminescence measurements, Optik 158 (2018) 237–242.
[55] S.N. Menon, B.S. Dhabekar, Sonal Kadam, D.K. Koul, Fading studies in $LiMgPO_4$: Tb, B and synthesis of new LiMgPO4 based phosphor with better fading characteristics, Nucl. Instrum. Methods Phys. Res., Sect. B 436 (2018) 45–50.